

## Article

# Fe-Cu-Zn Isotopic Compositions in Polymetallic Sulfides from Hydrothermal Fields in the Ultraslow-Spreading Southwest Indian Ridge and Geological Inferences

Yan Wang <sup>1,2</sup>, Zhongwei Wu <sup>2,3</sup>, Yi Huang <sup>1,\*</sup>, Xiaoming Sun <sup>2,4,\*</sup> , Jinhui Yan <sup>1</sup>, Fan Yang <sup>1</sup>, Zhengxin Yin <sup>5</sup> and Li Xu <sup>2</sup>

- <sup>1</sup> South China Sea Institute of Planning and Environmental Research, SOA, Guangzhou 510300, China; we85289786@163.com (Y.W.); yanjh@scs.mnr.gov.cn (J.Y.); yangfan@scs.mnr.gov.cn (F.Y.)
- <sup>2</sup> School of Marine Sciences, Guangdong Provincial Key Laboratory of Marine Resources and Coastal Engineering, Sun Yat-Sen University, Zhuhai 519082, China; figowzwpig@163.com (Z.W.); xu-bluesky@126.com (L.X.)
- <sup>3</sup> School of Jewelry and Art Design, Wuzhou University, Wuzhou 543002, China
- <sup>4</sup> School of Earth Sciences and Engineering, Sun Yat-Sen University, Zhuhai 519082, China
- <sup>5</sup> South China Sea Marine Survey and Technology Center, State Oceanic Administration, Guangzhou 510300, China; yinzhengxin@smst.gz.cn
- \* Correspondence: huangy@scs.mnr.gov.cn (Y.H.); eessxm@mail.sysu.edu.cn (X.S.); Tel.: +86-020-84219249 (Y.H.); +86-020-84110968 (X.S.)

**Abstract:** Submarine hydrothermal sulfides from the ultraslow-spreading Southwest Indian Ridge (SWIR) were sampled from three hydrothermal fields, and the Fe-Cu-Zn isotopic compositions were analyzed in this study. The Fe isotopes ranged from  $-0.011\%$  to  $-1.333\%$ . We believe the processes controlling the Fe isotope variability in the hydrothermal systems include the sulfide precipitation process, the initial isotopic composition of the hydrothermal fluid, and the temperature during precipitation. Among these factors, the sulfide precipitation process is the dominant one. The Cu isotope compositions of the sulfides varied from  $-0.364\%$  to  $0.892\%$ , indicating that the hydrothermal fluid preferentially leached  $^{65}\text{Cu}$  in the early stages and that hydrothermal reworking led to decreases in the Cu isotopes in the later stages. In addition, because mass fractionation occurred during sulfide precipitation, the Zn isotope variations ranged from  $-0.060\%$  to  $0.422\%$ . Combined with the S isotopic compositions, these results also implied that different Fe-Cu-Zn isotopic fractionation mechanisms prevailed for the different sample types. Based on these results, we are sure that the metallic elements, including Fe, Cu, and Zn, were derived from the mantle in the SWIR hydrothermal field, and the Fe-Cu isotope results indicated that these metallic elements were provided by fluid leaching processes. Using the isotopic fractionation and sulfide results, we calculated that the Fe-Cu-Zn isotopic compositions of the hydrothermal fluid in this field were  $\delta^{56}\text{Fe}_{(\text{fluid})}$ :  $-0.8\sim 0.0\%$ ;  $\delta^{65}\text{Cu}_{(\text{fluid})}$ :  $0.3\sim 1.3\%$ ; and  $\delta^{66}\text{Zn}_{(\text{fluid})}$ :  $0\sim 0.48\%$ .

**Keywords:** Fe-Cu-Zn isotope; isotopic fractionation; submarine hydrothermal sulfide; SWIR



**Citation:** Wang, Y.; Wu, Z.; Huang, Y.; Sun, X.; Yan, J.; Yang, F.; Yin, Z.; Xu, L. Fe-Cu-Zn Isotopic Compositions in Polymetallic Sulfides from Hydrothermal Fields in the Ultraslow-Spreading Southwest Indian Ridge and Geological Inferences. *Minerals* **2023**, *13*, 843. <https://doi.org/10.3390/min13070843>

Academic Editor: Georgy Cherkashov

Received: 28 May 2023

Revised: 17 June 2023

Accepted: 20 June 2023

Published: 22 June 2023



**Copyright:** © 2023 by the authors. Licensee MDPI, Basel, Switzerland. This article is an open access article distributed under the terms and conditions of the Creative Commons Attribution (CC BY) license (<https://creativecommons.org/licenses/by/4.0/>).

## 1. Introduction

Submarine hydrothermal sulfide deposits are widely distributed in global oceans and are rich in metallic elements, such as Cu, Zn, Pb, Au, and Ag; so, they are of great economic value and strategic significance [1–7]. Hydrothermal systems in the Southwest Indian Ridge (SWIR) are characterized by ultraslow spreading speeds compared to the other mid-ocean ridge hydrothermal systems [7–11]. The published papers have reported studies on the hydrothermal sulfides from the SWIR. However, they mainly focused on mineralogy and elemental geochemistry [8,12,13], and many problems were not reasonably explained, such as the metallogenic environment and the source and contribution mechanism of metallogenic materials. In summary, these hydrothermal systems in the SWIR have received

less attention than the extensively investigated hydrothermal systems in the Pacific Ocean and the Atlantic Ocean and in back-arc basins [6,14,15].

To address the above issues, we can apply multiple isotope systems, which indicate the sources of the metallogenic material, the evolutionary processes and the physical and chemical changes occurring in the fluid, to study the ore-forming process synthetically. Base metals (such as Fe, Cu, and Zn) are widely distributed in mineralized rocks and fluids and play important roles in diagenesis, metallogenesis, and hydrothermal activities. If we could study the Fe-Cu-Zn isotopic compositions directly, we would gather more clues and evidence revealing the different geologic processes occurring in nature [16]. Additionally, with the advent of multi-collector inductively coupled plasma mass spectrometry (MC-ICPMS) in recent years, the stable Fe-Cu-Zn isotope variability has been measured with high accuracy [17–20]. As a result, Fe, Cu, and Zn isotopes have been used frequently to trace the ore-forming fluid paths and the sources of the hydrothermal systems [19,21–23]. Thus far, the Fe isotopic compositions of seafloor hydrothermal sulfides and fluids have been determined for the East Pacific Rise (EPR), Juan de Fuca Ridge, and Mid-Atlantic Ridge, and they indicated an Fe isotopic fractionation mechanism operating in the hydrothermal systems [21,24–32]. In addition, Cu and Zn isotopes have been used extensively to study the metallogenic mechanisms of hydrothermal areas in the Mid-Atlantic Ridge, East Pacific Rise, and western Pacific back-arc basin [19,30,33–39].

Few studies have reported transition metal isotopes for the SWIR hydrothermal systems. Zeng et al. [30] and Li et al. [40] have reported sporadic Fe isotope data of the SWIR hydrothermal sulfides, but Cu and Zn isotope analyses are lacking. On the other hand, Fe, Cu, and Zn are ore-forming elements; so, it is more reasonable to trace the origins of the ore-forming elements by studying the Fe-Cu-Zn isotopes. As a result, we sought to measure the isotopes of these ore-forming elements directly and to combine the information with that for S isotopes to further understand the Fe-Cu-Zn isotope fractionation and the metallogenic environment. In addition, because these sulfides precipitated directly from the hydrothermal fluid, the origin of the ore-forming fluid can be traced by studying the isotopic compositions of the hydrothermal sulfides.

## 2. Geologic Setting

The Southwest Indian Ridge (SWIR) extends from the Bouvet triple junction (BTJ) at 55° S, 00° 40' W to the Rodrigues triple junction (RTJ) at 25° 30' S, 70° E (Figure 1), forming a boundary between the African and Antarctic plates with a length of approximately 8000 km. The SWIR spreads at the much slower rate of 13–18 mm/a; so, it is a typical ultraslow-spreading ridge [10]. Furthermore, some segments of the ridge lie at high angles relative to the regional spreading direction. The eastern section of the SWIR (25–70° E) is characterized by the Indomed, Gallieni, and Melville fracture zones, which exhibit a relatively uniform spreading rate of 14 mm/a. On the other hand, the western section of the SWIR (0–25° E) exhibits an average spreading rate of approximately 16 mm/a, which can be divided into two parts, 0–9° E, 9–16° E and 16–25° E, based on the spreading geometry [41]. From 0° E to 9° E, well-defined short ridge segments are offset by relatively long-lived transform faults, which lie orthogonal to the regional spreading direction. In contrast, the segmentation is poorly defined along the 400 km long section of the ridge between 9° and 16° E. This portion of the SWIR lies at a high angle relative to the regional spreading direction. As a result, this SWIR section has an effective spreading rate of only 4.2 mm/a, which is the slowest rate along the accessible portion of the global ridge system. Between 16° and 25° E, this portion of the SWIR is orthogonal to the regional spreading direction and is composed of a series of short segments separated by nontransform offsets [42]. In some segments, such as those around the transform faults, a significant amount of mantle material is exposed, such as serpentized peridotite. Some gabbros appears at the bottom of some great fractures [43].

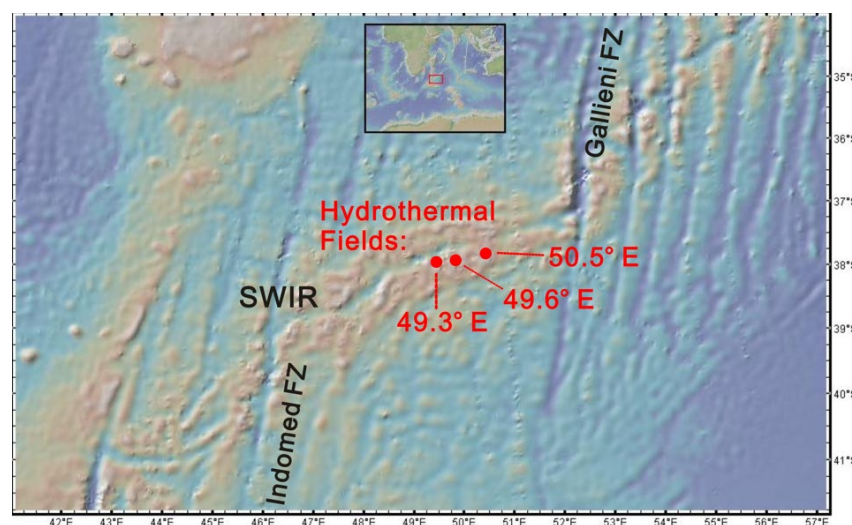


**Figure 1.** Location map of the study area on the Southwest Indian Ridge (between the Indomed and Gallieni fracture zones (FZs)) as well as the Central Indian Ridge (CIR) north of the Rodriguez triple junction (RTJ). The inset shows the regional setting of the ultraslow-spreading SWIR. For more detailed bathymetry and topography data of each of these six hydrothermal fields (marked with red circles), please see previous publications [44–53].

Our study was based on a collection of samples taken from the eastern section of the SWIR at 49–50° E; this is located between the Indomed fracture zone (Indomed FZ) and the Gallieni fracture zone (Gallieni FZ) (Figure 1), where investigations of the hydrothermal activity in the SWIR are the most advanced at present. Since 8–10 Ma, this segment of ridge has developed a suddenly increased melt-supplying process. This hypothesis has been proven by the shallower depth of seawater at both the axis of the ridge and the off-axis and the increased thickness of the crust compared with the other ridge areas [54]. It is known that the interaction between the Crozet hotspots and the SWIR is the result of abnormal ridge accretion; however, the pattern and process have been argued about [55]. Geophysical investigations have shown that the central section of the ridge is the highest melt-supplying area, where many flat-top volcanoes are developed, rift valleys disappear, and the shallowest seawater depth is 1570 m. On both sides of the ridge, the depths are greater and extend to the Indomed and Gallieni transform faults, respectively.

### 3. Samples and Methods

Our samples were obtained during the Chinese research cruise, which was supported by the China Ocean Mineral Resources Research and Development Association (COMRA). Samples of the hydrothermal sulfides, including those from S27-4, S35-22, S35-17, S7-4, and S25-21, and the hydrothermal sediments (S6-3) were obtained by TVG (television video-guided grab). Among them, S35-22, obtained from the Yuhuang hydrothermal field, is an Fe-Cu-rich massive sulfide sample, consisting mostly of subhedral pyrite/marcasite chalcopyrite with minor sphalerite. S27-4 is a Zn-rich massive sulfide sample, consisting mostly of euhedral/subhedral sphalerite and wurtzite; S7-4 is an Fe-rich relict chimney debris sample; S6-3 is a metalliferous sediment sample; and S35-17 is a black smoker chimney fragment containing anhedral pyrite and sphalerite and minor chalcopyrite; these were obtained from the Longqi hydrothermal field. S25-21 is an Fe-Cu-rich relict sulfide talus sample from the Tianzuo hydrothermal field and is principally composed of pyrite, bornite, and isocubanite. Fe-oxyhydroxides fill in the microcavities or fractures, which appear to have undergone extensive hydrothermal alteration and supergene weathering. Reflected-light and SEM photomicrographs for some of the samples can be found in Wang et al. [56].

In addition, three hydrothermal sulfide samples (EPR-1, EPR-2, and S4-1) from the East Pacific Rise (EPR) were studied for comparison. All the information on the samples is

shown in Table 1. The hydrothermal sulfides were ground into small particles with sizes of 0.2~0.5 mm. Then, these sulfide particles were dried at room temperature and sieved through a nylon griddle. To obtain homogeneous microcrystalline groundmass separates, various types of metal sulfides (approximately 2 g) with small diameters, such as pyrite, chalcopyrite, and sphalerite, were sieved and carefully hand-picked under a binocular microscope for Fe-Cu-Zn isotope analyses. Finally, these particles were ground into powders with sizes of 0.08~0.05 mm in an agate mortar. Notably, during the whole process non-metallic products were used to avoid pollution of the Fe-Cu-Zn isotope compositions with metallic products.

**Table 1.** Sample information and analytical projects <sup>1</sup>.

Vent Field	Sample ID	Longitude/Latitude	Depth (m)	Sample Description	Mineralogy	Isotopic Analysis
Yuhuang	S35-22	49.2° E/37.9° S	1445	Fe-Cu-rich massive sulfide	Py-Cpy-Po	Fe-Cu-Zn
	S27-4	49.6° E/37.8° S	2781	Zn-rich massive sulfide	Sp-Wur-Py	Fe-Cu-Zn
Longqi	S7-4	49.6° E/37.8° S	2755	Fe-rich relict chimney debris	Py-Mrc-Sp	Fe-Cu-Zn
	S6-3	49.6° E/37.8° S	2777	Metalliferous sediment	Py-Gth-Hem	Fe-Cu-Zn
	S35-17	49.6° E/37.8° S	2783	Black smoker chimney fragment	Py-Sp-Cpy	Fe-Zn
Tianzuo	S25-21	63.5° E/37.7° S	3666	Fe-Cu-rich relict sulfide talus	Py-Bn-Iso	Fe-Cu-Zn
EPR 13° N	EPR-1	EPR 13° N	2628	Fe-rich massive sulfide	Py-Mrc-Sp	Fe-Cu
	EPR-2	EPR 13° N	2633	Fe-rich massive sulfide	Py-Mrc-Sp	Fe-Cu
Niaochao	S4-1	Nearby EPR 0°	2747	Fe-Cu-rich massive sulfide	Py-Mrc-Cpy	Fe-Cu-Zn

<sup>1</sup> Py—pyrite; Cpy—chalcopyrite; Sp—sphalerite; Wur—wurtzite; Bn—bornite; Iso—isocubanite; Mrc—marcasite; Gth—goethite; Hem—hematite.

These powder samples were sent to the isotopic laboratory of the ALS Laboratory Group in Switzerland for Fe-Cu-Zn isotope analyses. We used hydrochloric acid and nitric acid to dissolve the sulfides. First, these samples were dissolved in dilute hydrochloric acid for 3 h. After centrifugal separation, the residual samples were dissolved in nitric acid. These solution samples were evaporated to dryness and dissolved in hydrochloric acid again. They were further purified for mass spectrometry by anion exchange chromatography. After sample pretreatment, we used a multi-collector inductively coupled plasma mass spectrometer (MC-ICPMS) with a Neptune-type flow meter to measure the Fe-Cu-Zn isotopic compositions. For more details on the analytical methods, please refer to Pérez et al. [57] and Rodushkin et al. [58]. The Fe-Zn isotopic reference materials, IRMM-014 and IRMM-3702, which were provided by the Institute of Reference Material and Measurements in Geel, Belgium, were employed as standards for the measurements of the Fe and Zn isotope ratios, respectively. The Cu isotopic compositions were determined relative to a Cu standard, such as NIST 976, which was provided by the American National Institute of Standards and Technology. The Fe-Cu-Zn isotopic compositions were expressed as  $\delta^{56}\text{Fe}$ ,  $\delta^{57}\text{Fe}$  ( $\delta^{56}\text{Fe} \approx 0.68 \times \delta^{57}\text{Fe}$ ),  $\delta^{65}\text{Cu}$ , and  $\delta^{66}\text{Zn}$  and calculated as a deviation relative to the standard with the following equations:

$$\Delta^{56}\text{Fe} = [({}^{56}\text{Fe}/{}^{54}\text{Fe})_{\text{sample}} / ({}^{56}\text{Fe}/{}^{54}\text{Fe})_{\text{IRMM-14}} - 1] \times 1000$$

$$\delta^{57}\text{Fe} = [({}^{57}\text{Fe}/{}^{54}\text{Fe})_{\text{sample}} / ({}^{57}\text{Fe}/{}^{54}\text{Fe})_{\text{IRMM-14}} - 1] \times 1000$$

$$\delta^{65}\text{Cu} = [({}^{65}\text{Cu}/{}^{63}\text{Cu})_{\text{sample}} / ({}^{65}\text{Cu}/{}^{63}\text{Cu})_{\text{NIST976}} - 1] \times 1000$$

$$\delta^{66}\text{Zn} = [({}^{66}\text{Zn}/{}^{64}\text{Zn})_{\text{sample}} / ({}^{66}\text{Zn}/{}^{64}\text{Zn})_{\text{IRMM-3702}} - 1] \times 1000$$

#### 4. Results

As previously mentioned, IRMM-014, NIST 976, and IRMM-3702 were used as standards for the Fe-Cu-Zn isotopic analyses. The results are shown in Table 2. To check the reliability and accuracy, a linear relationship between the natural log of  $\delta^{56}\text{Fe}/\delta^{57}\text{Fe}$  and  $\delta^{66}\text{Zn}/\delta^{68}\text{Zn}$  is used to determine the mass bias relationships (Figure 2). We found that the slopes for the Fe and Zn isotopic analyses were 1.493 and 1.992, respectively, and were consistent with the results of Beard et al. [20] and John et al. [22], and they were also in

agreement with the differences caused by isotope mass fractionation. This indicated that most of the jamming signals were reduced in the analyses, especially for the nuclear isobars.

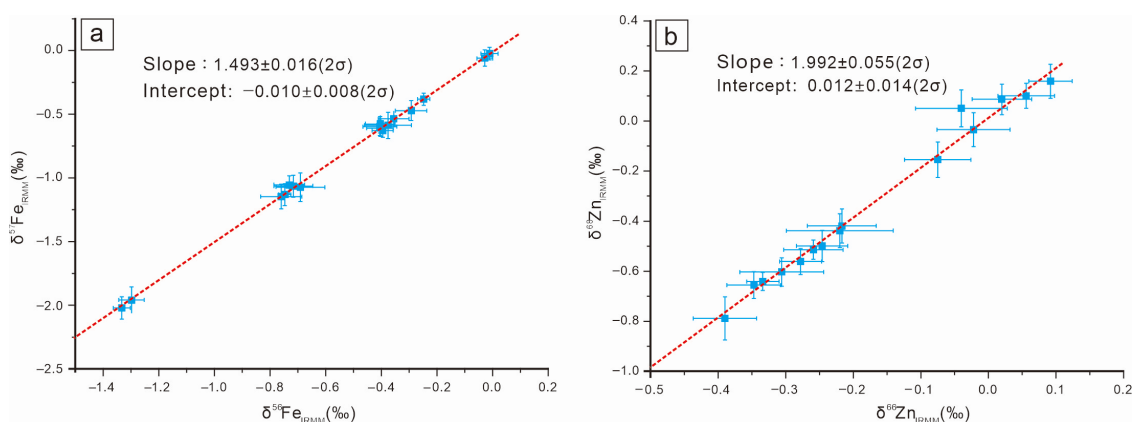


**Figure 2.** Linear regression fitting line diagram of  $\delta^{56}\text{Fe}$ - $\delta^{57}\text{Fe}$  (a) and  $\delta^{66}\text{Zn}$ - $\delta^{68}\text{Zn}$  (b).

IRMM-3702 was used as the Zn isotopic standard in this analysis, but previous studies commonly used the JMC Zn solution (finished) as the standard. Therefore, we converted the results to the JMC Zn solution standard to facilitate a comparison. The formula used was:

$$\delta^{66}\text{Zn}_{\text{IRMM-3702}} \approx -0.33 + \delta^{66}\text{Zn}_{\text{JMC}} \text{ [59].}$$

The results shown in Table 2 are those obtained after the conversion.

## 5. Discussion

### 5.1. Fe Isotopes

As shown in Table 2, the Fe isotopic compositions in this study fell within a large range, with  $\delta^{56}\text{Fe}$  changing from  $-0.011$  to  $-1.333$ ‰ and  $\delta^{57}\text{Fe}$  changing from  $-0.024$  to  $-2.021$ ‰. We will focus on  $\delta^{56}\text{Fe}$  here to enable convenient discussions and comparisons. Table 2 and Figure 3 show that most of the  $\delta^{56}\text{Fe}$  values determined in this study fell within the range of those for global submarine hydrothermal sulfides ( $\delta^{56}\text{Fe}$ :  $0.42$ ~ $-2.13$ ‰ [21,24,27,28,60]). Compared with the average value for sulfide samples from the EPR ( $-0.349$ ‰), the hydrothermal sulfides from the SWIR showed a lower average value of  $-0.621$ ‰. In comparison with the Fe isotopic compositions in other geologic bodies (Table 2 and Figure 3), the submarine hydrothermal sulfides showed greater isotopic fractionation due to kinetic fractionation. However, the  $\delta^{56}\text{Fe}$  values for the SWIR displayed more concentrated results than those from Lucky Strike and EPR  $9$ – $10^\circ$  N, which agreed with the S isotopic results. The reason may lie in the geologic setting of the SWIR, which is an ultraslow-spreading and sediment-starved mid-ocean ridge without obvious biotic fractionation as a result. However, we cannot exclude the possibility that there are no low-temperature samples in this study. Figure 3 shows that the  $\delta^{56}\text{Fe}$  values in the SWIR approached the values of the mid-ocean ridge basalts (MORBs, approximately  $0.0$ ‰; [20]), indicating that Fe may be derived from the mantle and that the sulfide-forming process leads to Fe isotopic fractionation. This conclusion is in agreement with a He-Ar isotopic study [56]. When combined with the S isotopic compositions, there was an obvious positive correlation between the Fe and S isotopes in the sulfide samples from the SWIR and the Lucky Strike and EPR  $9$ – $10^\circ$  N hydrothermal fields (Figure 4), suggesting that the mechanisms for the formation of pyrite and chalcopyrite influenced the Fe-S isotopic compositions [60]. However, some samples showed a drift away from the positive correlation, indicating fractionation of the Fe-S isotopes and different fractionation mechanisms.

**Table 2.** Fe-Cu-Zn isotopic compositions of the hydrothermal sulfides studied herein <sup>1</sup>.

Sample	No.	Analyzed Mineral <sup>2</sup>	$\delta^{56}\text{Fe}$ (‰)	$\pm 1$ sd	$\delta^{57}\text{Fe}$ (‰)	$\pm 1$ sd	$\delta^{65}\text{Cu}$ (‰)	$\pm 1$ sd	$\delta^{66}\text{Zn}$ IRMM-3702 (‰)	$\pm 1$ sd	$\delta^{68}\text{Zn}$ IRMM-3702 (‰)	$\pm 1$ sd	$\delta^{68}\text{Zn}$ JMC (‰)	$\delta^{34}\text{S}$ (‰) <sup>4</sup>
S35-22	S35-22-1	Py	−0.011	0.031	−0.024	0.049	0.892	0.042	−0.040	0.068	0.051	0.074	0.290	4.8
	S35-22-2	W.R.	−0.028	0.028	−0.059	0.064	0.803	0.021	−0.022	0.054	−0.034	0.068	0.308	4.9
S27-4	S27-4-1	Sph	−0.376	0.084	−0.587	0.104	0.782	0.040	−0.306	0.062	−0.603	0.057	0.024	3.4
	S27-4-2	W.R.	−0.405	0.048	−0.608	0.060	0.798	0.038	−0.390	0.047	−0.789	0.086	−0.060	3.2
S35-17	S35-17-1	Py	−1.298	0.046	−1.959	0.105	-	-	−0.278	0.031	−0.561	0.052	0.052	4.1
	S35-17-2	Sph	−1.333	0.031	−2.021	0.088	-	-	−0.217	0.051	−0.419	0.068	0.113	4.3
S7-4	S7-4	W.R.	−0.747	0.022	−1.131	0.086	0.634	0.021	−0.220	0.079	−0.154	0.071	0.110	5.5
S6-3	S6-3	W.R.	−0.355	0.055	−0.536	0.063	0.316	0.032	−0.075	0.049	−0.438	0.068	0.255	7.5
	S25-21-1 a	Py	−0.716	0.070	−1.065	0.086	−0.300	0.036	−0.246	0.038	−0.499	0.063	0.084	9.3
S25-21 <sup>3</sup>	S25-21-1 b	Py	−0.731	0.055	−1.056	0.073	−0.349	0.042	−0.259	0.044	−0.514	0.039	0.071	9.8
	S25-21-2 a	W.R.	−0.760	0.074	−1.146	0.098	−0.364	0.033	−0.334	0.024	−0.641	0.036	−0.004	8.4
	S25-21-2 b	W.R.	−0.691	0.088	−1.074	0.112	−0.341	0.033	−0.347	0.040	−0.655	0.054	−0.017	-
EPR-1	EPR-1	Py	−0.395	0.038	−0.629	0.052	0.150	0.038	-	-	-	-	-	3.5
EPR-2	EPR-2	Py	−0.293	0.056	−0.472	0.080	−0.537	0.030	-	-	-	-	-	-
	S4-1-1	Py	−0.248	0.022	−0.383	0.047	−0.008	0.036	0.092	0.032	0.159	0.068	0.422	5.5
S4-1	S4-1-2 a	W.R.	−0.404	0.053	−0.577	0.071	−0.127	0.030	0.020	0.044	0.087	0.061	0.350	3.8
	S4-1-2 b	W.R.	−0.405	0.061	−0.596	0.077	−0.132	0.031	0.056	0.042	0.101	0.050	0.386	-

<sup>1</sup> “-” means untested. <sup>2</sup> The mineral abbreviations are shown in Table 1, and W.R. stands for whole rock. <sup>3</sup> Parallel samples are marked as “a” and “b” for distinction. <sup>4</sup> S isotope compositions were derived from the published literature [56] and unpublished data.

Rouxel et al. [60] discussed the possible processes controlling Fe isotope variability in hydrothermal fluids, including phase separation, high-temperature basalt alteration, and subsurface processes. Among these processes, Beard et al. [26] found no more than a 0.15% difference between the Fe isotope compositions of the vapor and the brine phases derived from phase separation. Rouxel et al. [21] observed significant Fe isotopic fractionation in secondary Fe-bearing minerals (e.g., celadonite and Mg-Fe amphibole) formed during both low- and high-temperature alterations. Highly altered basalts that were depleted in Fe, however, displayed an increase in  $\delta^{56}\text{Fe}$  values relative to the fresh values, which suggested preferential leaching of the light Fe isotopes (between  $-0.5$  and  $-1.3\text{‰}$ ) during alteration. As a result, hydrothermal alteration fluids can exhibit relatively negative Fe isotopic compositions. In addition, as suggested by Rouxel et al. [60], significant Fe isotopic fractionations in hydrothermal fluids may also occur during Fe-sulfide precipitation in subsurface environments. Using the Fe isotopic compositions of the hydrothermal sulfides from EPR 9–10° N, Rouxel et al. [60] found that in the case of relatively slow pyrite precipitation in subsurface environments caused by conductive cooling of the fluids, limited Fe isotopic fractionation was observed; in contrast, when rapid precipitation of pyrite occurred as a result of mixing with seawater, as is typical of chimney environments, significant kinetic Fe isotope fractionation was expected. At the same time, the study by Rouxel et al. [21] on the Lucky Strike hydrothermal fields showed that the hydrothermal sulfide precipitates had lower  $\delta^{56}\text{Fe}$  values as the temperatures of the fluids decreased. Based on the previous study, therefore, the author believes that Fe isotopic compositions in hydrothermal sulfides are controlled by the initial isotopic composition in the hydrothermal alteration fluids, the sulfide precipitation process, and the precipitation temperature. Accordingly, we can analyze and discuss the Fe isotopic compositions and fractionation in the SWIR hydrothermal sulfides.

In the SWIR hydrothermal sulfides, most of the  $\delta^{56}\text{Fe}$  values fell within the range of  $-0.355$  and  $-0.760\text{‰}$ , except for S35-17 and S35-22. Because S35-17 was a black smoker sample, it was derived from the rapid precipitation of the sulfides produced by the mixing of hydrothermal fluids and seawater. In this environment, rapid precipitation of the sulfides produced by the mixture led to significant kinetic Fe isotopic fractionation (approximately  $-1.5\text{‰}$ , [66]). As a result, this conclusion was highly consistent with the  $\delta^{56}\text{Fe}$  values for S35-17 ( $-1.298\sim-1.333\text{‰}$ ), suggesting that the kinetic isotopic fractionation led to much more negative  $\delta^{56}\text{Fe}$  values in this sample. For S35-17, we found that the  $\delta^{56}\text{Fe}$  of the sphalerite ( $-1.333\text{‰}$ ) formed from low temperatures in the outer zone was lower than that of the high-temperature pyrite ( $-1.298\text{‰}$ ) from the inner zone. This confirmed the conclusion that a temperature reduction led to a decrease in  $\delta^{56}\text{Fe}$ . On the other hand, in the massive sulfide samples, such as S27-4, S25-21, and S7-4, the  $\delta^{56}\text{Fe}$  values were slightly negative, ranging from  $-0.355$  to  $-0.760\text{‰}$ . As in the previous results reported by Rouxel et al. [60], when the hydrothermal fluid was isolated from the seawater in the subsurface environment, conductive cooling led to the formation of massive sulfides through multiple remineralization stages and produced sulfides with  $\delta^{56}\text{Fe}$  values that were near to isotopic equilibrium with the fluids (so, the Fe isotopic compositions of the massive sulfides fell in the hydrothermal fluid area in Figure 4). As a result, the  $\delta^{56}\text{Fe}$  values of the hydrothermal fluids were inferred to be slightly negative and similar to those of the massive sulfides; this was consistent with the fractionation effects of basalt alteration, suggesting that the Fe was derived from basalt alteration and leaching processes. This conclusion can be verified by the discovery of altered minerals (e.g., celadonite) in the basalt samples from around these areas [67]. In contrast, S35-22, which contained more high-temperature minerals (e.g., chalcopyrite), showed higher  $\delta^{56}\text{Fe}$  values ( $-0.011$  and  $-0.028\text{‰}$ ) than the other massive sulfides, such as S27-4, S25-21, and S7-4, inferring that the higher  $\delta^{56}\text{Fe}$  values in this sample were related to the higher initial isotopic composition and precipitation temperature. Under high-temperature conditions,  $^{56}\text{Fe}$  and  $^{57}\text{Fe}$  are more easily absorbed by chalcopyrite [68]. Thus, chalcopyrite formed at high temperatures has higher  $\delta^{56}\text{Fe}$  values. As a result, S35-22 with a higher  $\delta^{56}\text{Fe}$  is related to higher formation temperatures.

In Figure 3, the average  $\delta^{56}\text{Fe}$  values for chalcopyrite from the major hydrothermal fields were higher than the average values for pyrite and sphalerite.

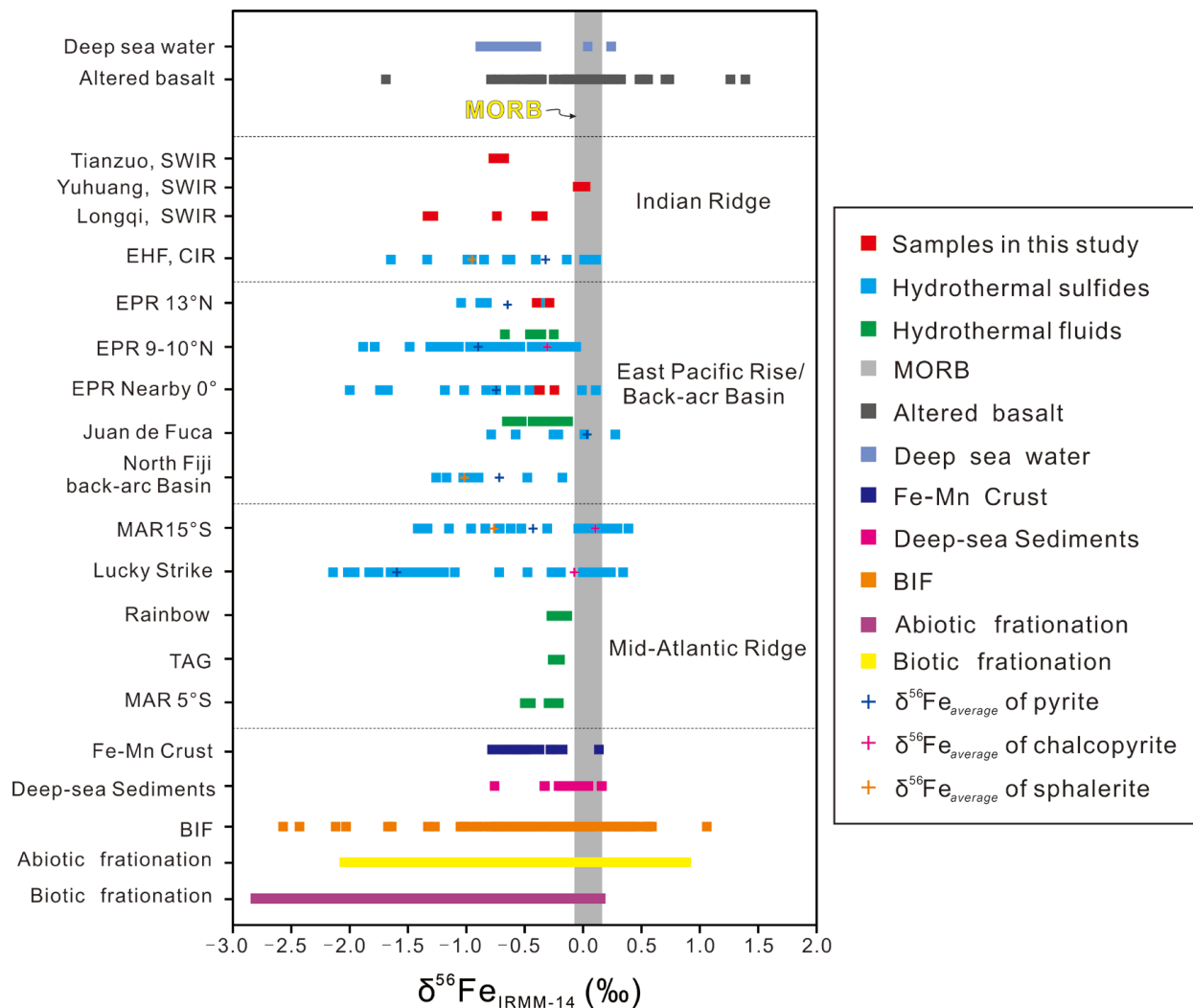


**Figure 3.** Contrast of the Fe isotopic ratios in sulfide samples taken from different hydrothermal fields, compared with the Fe isotopic ratios in iron-manganese concretion, BIF, abiotic, and biotic fractionation (data are from the published literature [21,24,27–32,40,60–65]).

In conclusion, the Fe in the SWIR hydrothermal sulfides was mainly derived from the oceanic crusts and upper mantle mafic–ultramafic source rocks (such as typical MORBs and/or gabbros). The Fe input contribution from the seawater end-member and deep-sea sediments can be considered negligible. However, the Fe isotopic fractionation in the samples depended on the precipitation mechanism, the initial isotopic composition, and the precipitation temperature. The precipitation mechanism played a more important role in the Fe isotopic fractionation, as indicated by comparing the black smoker sample (S35-17) with the massive sulfide samples (S27-4, S35-22). Moreover, the chalcopyrite-rich sample (S35-22) had a higher  $\delta^{56}\text{Fe}$  because of the higher formation temperature.

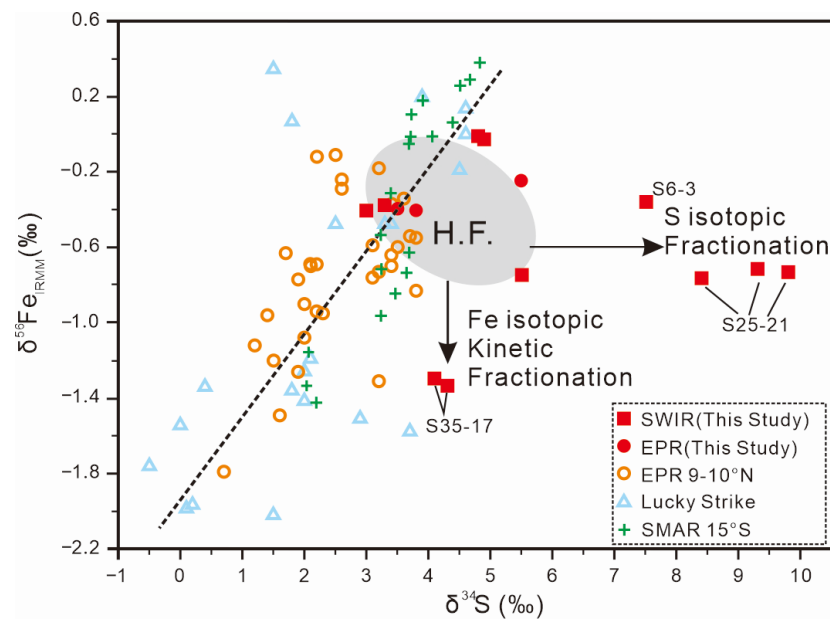


**Figure 4.**  $\delta^{56}\text{Fe}$  vs.  $\delta^{34}\text{S}$  plots for hydrothermal sulfides from the SWIR and the other hydrothermal fields. The sulfur isotopic compositions of S6-3 and S25-21 samples were previously reported by Wang et al. [56] (data for EPR 9–10° N, Lucky Strike, SMAR 15° N, and hydrothermal fluids (H.F.) are from the published literature [21,24,29,60]).

## 5.2. Cu Isotopic Results and Discussion

The Cu isotopic compositions in this study varied from  $-0.364$  to  $0.892\text{‰}$ , as shown in Table 2, and fell primarily within the Cu isotopic composition range for global submarine hydrothermal sulfides ( $\delta^{65}\text{Cu}$ :  $-0.98$ – $3.14\text{‰}$ ; Figure 5; [19,30,33]). The hydrothermal sulfide samples from the SWIR had an average  $\delta^{65}\text{Cu}$  value of  $0.287\text{‰}$ , while the average  $\delta^{65}\text{Cu}$  value for the samples from the EPR around the equator was  $-0.089\text{‰}$ . In comparison with the data for the other hydrothermal fields in the world, the  $\delta^{65}\text{Cu}$  values of the SWIR samples, which ranged from  $-0.364$  to  $0.892\text{‰}$ , were consistent with those in the Lucky Strike hydrothermal field from the Atlantic Ocean and more concentrated than those in the Logatchev and Rainbow hydrothermal fields from the Atlantic Ocean. In contrast with the other deposit types, the  $\delta^{65}\text{Cu}$  values for the SWIR hydrothermal sulfides were distributed in a range which was consistent with those of the VHMS and magmatic deposits, which were very close to the value of MORB (approximately  $0\text{‰}$ ; [69]) but far from the range for seawater ( $\delta^{65}\text{Cu}$ :  $0.9$ – $1.5\text{‰}$ ; [70]), indicating that the Cu was mainly derived from the oceanic crusts and upper mantle mafic–ultramafic source rocks. The range of  $\delta^{65}\text{Cu}$  values in the EPR samples was much more concentrated because there were fewer samples and the samples also included those from previous studies [19]. The S isotopic compositions show that this is very different from the situation with the Fe–S isotopes in that there was no positive correlation between  $\delta^{65}\text{Cu}$  and  $\delta^{34}\text{S}$  in most of the hydrothermal sulfides (Figure 6). This suggests that the Cu isotopic compositions were less affected by sulfide (chalcopyrite) precipitation than the Fe isotopes.

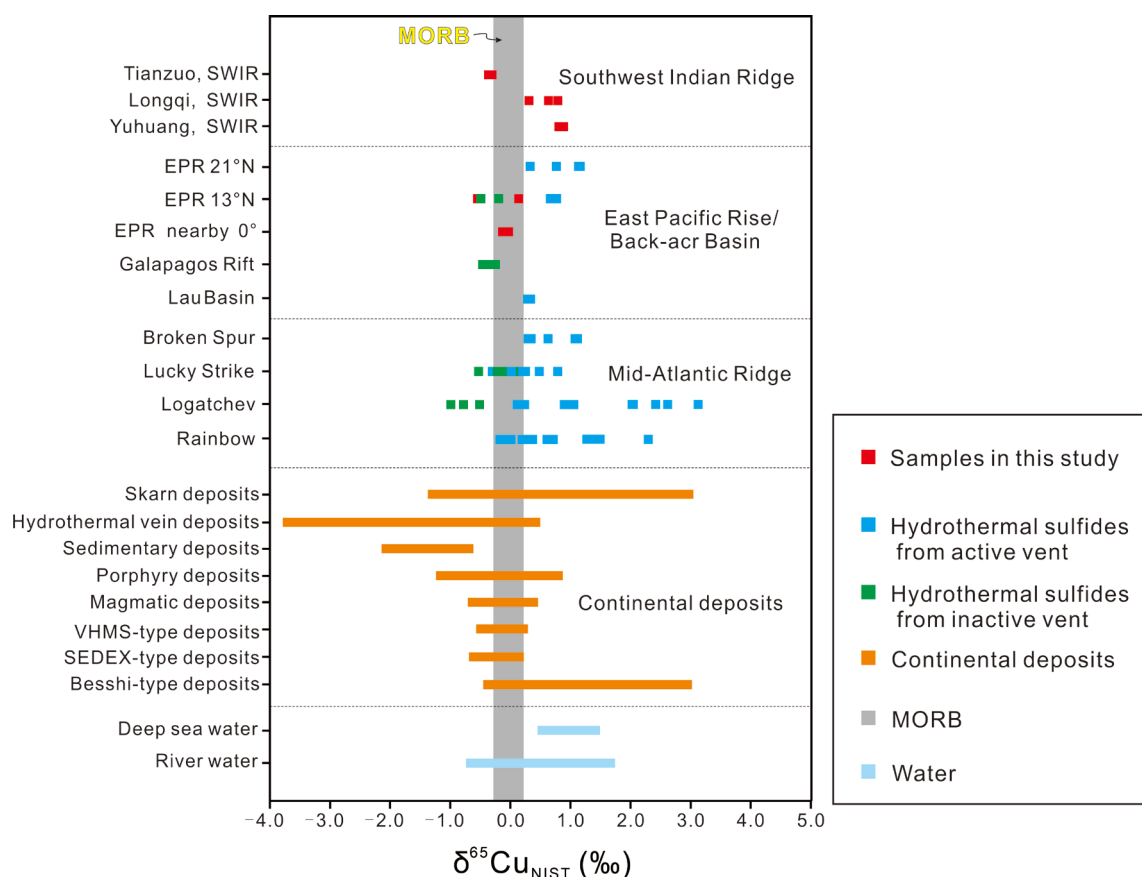


**Figure 5.** Comparison of Cu isotopic ratios for sulfide samples from different hydrothermal fields, compared with Cu isotopic ratios for different types of deposits (data are from the published literature [19,23,33,69–81]).

As indicated in a previous study of high-temperature hydrothermal systems by Rouxel et al. [33], copper isotopes can be fractionated by a variety of processes: (1) during leaching of copper from basalts; (2) during precipitation; (3) by hydrothermal reworking of copper sulfides below the seafloor by hydrothermal vents; and (4) by late-stage processes occurring at low temperatures. Zhu et al. [19] thought that Cu isotopic fractionation was different from Fe isotopic fractionation in the leaching processes since  $^{65}\text{Cu}$  was preferentially leached from the basalt source and not relevant to the source rock; this caused the early-stage fluids to display higher  $\delta^{65}\text{Cu}$  values. In comparison with the Fe isotopes, subsea floor sulfide precipitation is not expected to kinetically fractionate the Cu isotopes effectively, and the  $\delta^{65}\text{Cu}$  values for the sulfides were therefore not affected [33]. However, the reworking process and alteration of the primary copper sulfides played more important roles in the Cu isotopic fractionation. During the reworking and alteration processes, the Cu isotopes were exchanged between early-stage copper sulfides enriched in  $^{65}\text{Cu}$  and late-stage hydrothermal fluid depleted in  $^{65}\text{Cu}$ . If heavy Cu was released during the reworking and alteration of the copper sulfides, the residual sulfides and inactive vents should have had their  $\delta^{65}\text{Cu}$  values shifted towards negative values as the replacement reactions proceeded. This feature was much more obvious for the sulfides from the Logatchev hydrothermal fields (Figure 5; [19,33]). On the other hand, secondary processes can lead to much higher  $\delta^{65}\text{Cu}$  values in secondary copper minerals because of periodic incursions by seawater. Synthesizing these factors indicates that the reworking and alteration of primary copper sulfides are the most common causes of Cu isotopic fractionation. In addition, in the study of the EPR hydrothermal area reported by Zhu et al. [19], the old inactive vent deposits were enriched in  $^{63}\text{Cu}$  and showed lower  $\delta^{65}\text{Cu}$  values and smaller variations relative to active high-temperature hydrothermal vents. These  $\delta^{65}\text{Cu}$

values were obviously lower than the average  $\delta^{65}\text{Cu}$  values of MORB ( $\delta^{65}\text{Cu}_{\text{average}}$ : 0.07‰, refs. [23,71]) and hydrothermal fluids ( $\delta^{65}\text{Cu}_{\text{average}}$ : 0.1‰~0.5‰, ref. [72]).

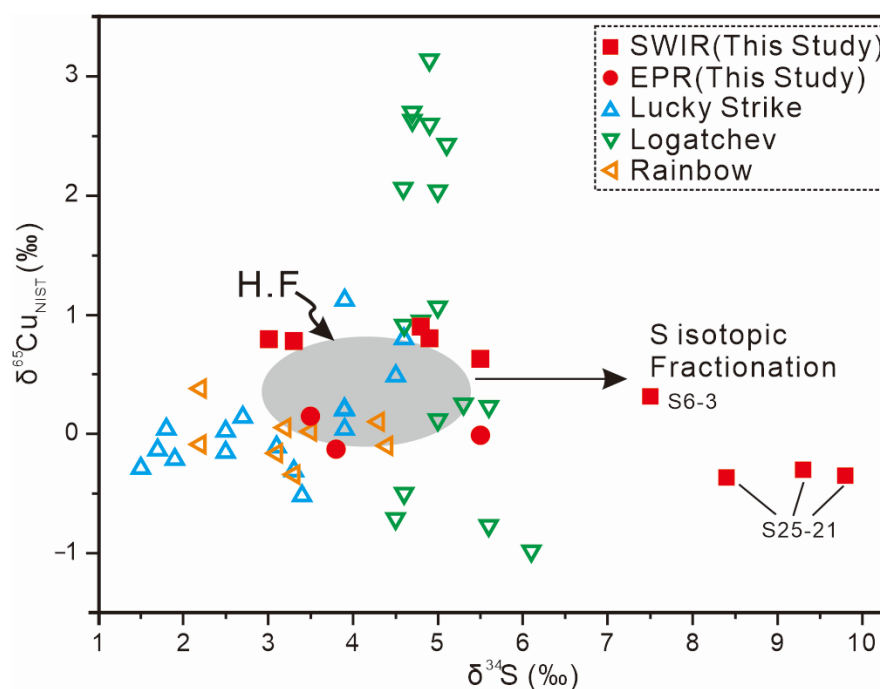


**Figure 6.**  $\delta^{65}\text{Cu}$  vs.  $\delta^{34}\text{S}$  plots for hydrothermal sulfides from the SWIR and the other hydrothermal fields (data for the Lucky Strike, Logatchev, and Rainbow and hydrothermal fluids (H.F.) are from Rouxel et al. [33] and Dekov and Rouxel [72], respectively).

Using the conclusion described above, the Cu isotopic compositions can now be discussed. The  $\delta^{65}\text{Cu}$  values for most of the SWIR hydrothermal sulfides fell within the range of 0.316 to 0.892‰, except for that of S25-21. Among these samples, S35-22 and S27-4 displayed relatively positive  $\delta^{65}\text{Cu}$  values, indicating that these samples were formed in an early stage. Because the early-stage hydrothermal fluids were enriched in  $^{65}\text{Cu}$  after the leaching of the basalt and through conductive cooling processes, these sulfides were produced and did not experience hydrothermal reworking processes in a later stage. Studies on the Au-Ag minerals in these samples also confirmed that the samples did not experience reworking and secondary enrichment processes [82]. In contrast, S6-3 showed a relatively low  $\delta^{65}\text{Cu}$  value of 0.316‰. The reason for this may be that this hydrothermal sediment sample formed in the late stage, when the  $\delta^{65}\text{Cu}$  value of the hydrothermal fluid had decreased. Together with the higher  $\delta^{65}\text{Cu}$  values in S27-4 and S7-4, the Cu isotopic compositions in the SWIR samples confirmed that the early-stage fluids were enriched in  $^{65}\text{Cu}$  and that the late-stage fluids were depleted in  $^{65}\text{Cu}$ . In comparison with the higher values seen for these samples, S25-21 displayed a negative Cu isotopic composition (−0.300~−0.364‰). We found that most of the primary Cu-Fe sulfides in this sample (such as high-temperature isocubanite) were characterized by typical replacement textures related to coupled dissolution–reprecipitation mechanisms [56], suggesting that this sample might have undergone late-stage hydrothermal reworking or post-depositional alteration (resulting from a long history of local hydrothermal activity), leading to a more negative  $\delta^{65}\text{Cu}$  value. The isotopic composition (1.12 Ra; [56]) in S25-21 also suggested that this sample underwent reworking processes as well. On the other hand, the S isotopic result for S25-21 [56] suggested that there was a large amount of seawater-derived S, resulting in the higher S isotopic composition and the inconsistency with the other samples in Figure 6. As a result, the reworking processes played important roles in the Cu-S isotopic fractionation. In addition, Cu isotopic mass fractionation also occurred between

different sulfides, and bornite was more enriched in the light isotopes than chalcopyrite [82]. In S25-21, bornite was one of the essential minerals (Table 1), and it showed relatively negative values in some ways. On the other hand, the EPR samples near 0° (S4-1) had  $\delta^{65}\text{Cu}$  values ( $-0.132\sim-0.008\text{‰}$ ) close to those of MORB, suggesting mantle-derived Cu. In contrast, the hydrothermal sulfides from EPR 13° N showed variable Cu isotopic compositions ( $-0.537\text{‰}$  and  $0.150\text{‰}$ ), which were close to those reported previously ( $\delta^{65}\text{Cu}$  for active hydrothermal vents:  $0.680\sim0.779\text{‰}$ ;  $\delta^{65}\text{Cu}$  for inactive hydrothermal vents:  $-0.482\sim-0.186\text{‰}$ ; [19]), and EPR-2 displayed a more negative value and might have been sampled from an inactive hydrothermal vent.

On the basis of the analysis provided above, the Cu in the SWIR hydrothermal sulfides was mainly derived from the mantle. However, Cu isotopic composition variations in the SWIR sulfides were explained with a two-stage model [19], which involved preferential leaching of  $^{65}\text{Cu}$  during the hydrothermal processes and resulted in the enrichment of heavy isotopes, while the reworking processes in the late stage resulted in Cu isotope decreases, such as in S25-21. As Seo et al. [83] showed, the vapor phase contained light copper isotopes preferentially leading to vapor fluids with negative  $\delta^{65}\text{Cu}$  values during the magmatic degassing processes, such as with the Qulong porphyry copper deposit in Tibet [84]. Yang and Scott [85] thought that magmatic degassing processes supplied metallic elements to the submarine hydrothermal systems in the Manus Basin. If the metallic elements were derived from magmatic degassing processes occurring in the SWIR hydrothermal system, as in Seo et al.'s [83] study, the primary copper sulfides precipitated from the vapor phase should display relatively negative  $\delta^{65}\text{Cu}$  values; this is inconsistent with the positive  $\delta^{65}\text{Cu}$  results found in this study. The metallic elements in the SWIR hydrothermal system were derived from leaching processes but not magmatic degassing processes, suggesting different metallogenic mechanisms for different hydrothermal fields.

### 5.3. Zn Isotopic Results and Discussion

As shown in Table 2, the Zn isotopic values fell within a narrow range and varied from  $-0.060$  to  $0.422\text{‰}$ . Therefore, in comparison with the Fe and Cu isotopes, there was less Zn isotopic fractionation. On the one hand, the samples from the EPR around the equator showed much higher  $\delta^{66}\text{Zn}$  values ( $0.350\sim0.422\text{‰}$ ), and the  $\delta^{66}\text{Zn}$  values for the samples from the SWIR ranged from  $-0.060$  to  $0.308\text{‰}$ , suggesting regional differences in Zn isotopic compositions. In contrast with the other hydrothermal systems (Figure 7), the results obtained in this study agreed with the values for the hydrothermal sulfides in the Bio 9 vent from EPR 9° N ( $-0.09\sim0.32\text{‰}$ ; [22]) and the hydrothermal fluids from the TAG hydrothermal systems ( $0\sim0.42\text{‰}$ ; [22]). Overall, in contrast to deep-sea sediments, the Zn isotopic ratios in the hydrothermal systems were close to the  $\delta^{66}\text{Zn}$  values in MORB, suggesting that Zn was derived from the mantle. Together with the S isotopic compositions, these results implied that there was an obvious positive correlation between the  $\delta^{66}\text{Zn}$  and  $\delta^{34}\text{S}$  values for the Fe and S isotopes (except for the samples influenced by seawater-derived S; Figure 8), suggesting that the mechanism for the formation of the Zn sulfides (sphalerite) affected Zn isotopic fractionation.

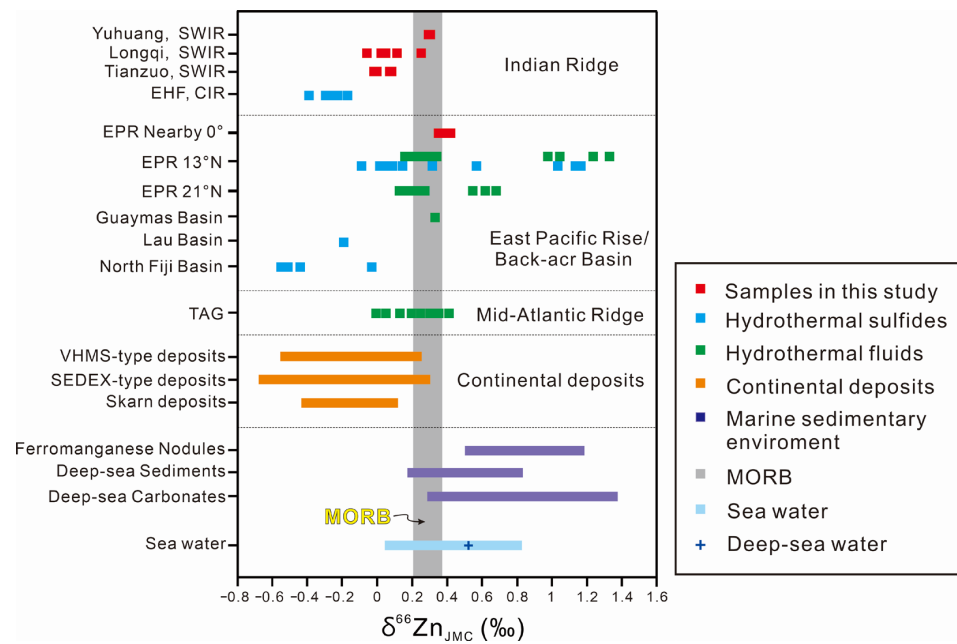


**Figure 7.** Comparison of Zn isotopic ratios for sulfide samples from different hydrothermal fields, compared with the Zn isotopic ratios for different types of deposits (data were from the published literature [17,22,86–91]).

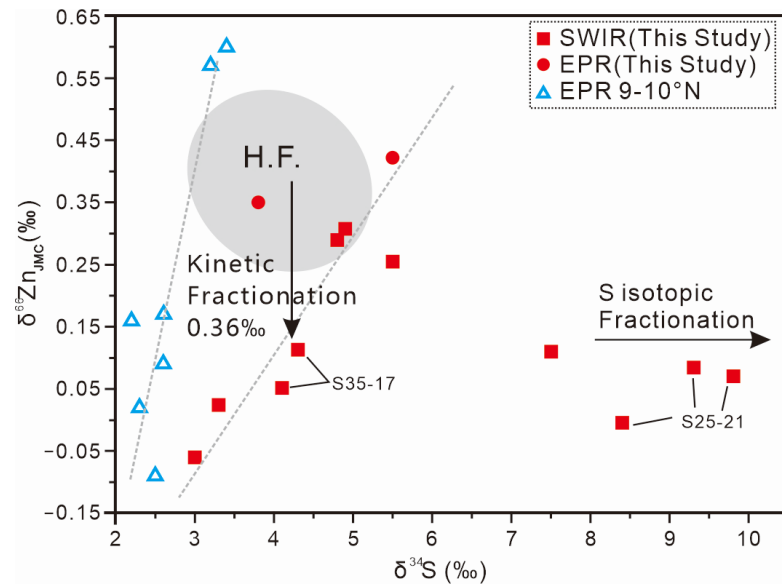


**Figure 8.**  $\delta^{66}\text{Zn}$  vs.  $\delta^{34}\text{S}$  plots for the hydrothermal sulfides from the SWIR and the other hydrothermal fields.

The data on the Zn isotope and S isotope of the sulfides in EPR 9–10° N were given by John et al. [22], respectively.

According to a previous study, several reasons can be invoked to explain the values of  $\delta^{66}\text{Zn}$  for the hydrothermal fluids, including differences in the source rock, fractionation occurring during phase separation, kinetic or equilibrium fractionation occurring during subsurface precipitation of Zn sulfides, and subsurface redissolution of Zn sulfides [22]. Because the total  $\delta^{66}\text{Zn}$  range for the fluids is an order of magnitude greater than that reported for basalt (0.20–0.30‰; [22]), the source rocks are unlikely to be the cause of the isotopic variability. Additionally, phase separation does not appear to be an important

factor in fractionating the Zn isotopes because no relationship was observed between chlorinity and  $\delta^{66}\text{Zn}$  in the hydrothermal fluids. As with the Fe isotopes, the precipitation of sulfides containing light Zn isotopes from the hydrothermal fluids is the main cause of the isotopic variation. Laboratory experiments have also demonstrated sulfide precipitation exhibiting an isotope effect of  $\Delta\delta^{66}\text{Zn} = -0.36\text{‰}$  [92]. Wilkinson et al. [93] suggested that the variation in Zn isotopes was most likely due to kinetic fractionation involving preferential incorporation of the light Zn isotopes in sphalerite precipitated rapidly under disequilibrium conditions. On the other hand, minimal or slightly positive Zn isotope fractionation factors (up to 0.1‰) for sphalerite and vent fluid could have resulted from near-equilibrium isotope effects affecting Zn-sulfide precipitation [22], such as conductive cooling. Moreover, Zn isotopic mass fractionation occurred for different sulfides during the formation process. Compared with pyrite and chalcopyrite, sphalerite was enriched in the heavier Zn isotopes [34]. Taking the VHMS deposit in the Ural area as an example, the  $\delta^{66}\text{Zn}$  value for the sphalerite-type samples was higher than that for the chalcopyrite-type samples by 0.4‰ [34]. In addition, the redissolution of Zn sulfides has not been tested in the laboratory; so, the fractionation mechanism is not clear.

On the basis of the studies described above, the  $\delta^{66}\text{Zn}$  values of the black smoker samples (S35-17) were 0.052‰ and 0.113‰, which may be explained by the kinetic fractionation resulting from rapid precipitation. When the results for Zn isotopic fractionations in laboratory experiments ( $-0.36\text{‰}$ ; [92]) were used to back-calculate the initial isotopic compositions of hydrothermal fluids, the value did not exceed 0.48‰, which was close to the  $\delta^{66}\text{Zn}$  values for the fluids from the TAG hydrothermal fields (0–0.42‰; [22]) and fell within the range for hydrothermal fluids (Figure 8, [22]); this shows that the source rocks were unlikely to be the reason for isotopic variability. In the massive sulfide samples (e.g., S35-22 and S4-1), the  $\delta^{66}\text{Zn}$  values were very close to the values calculated for the hydrothermal fluids, suggesting that the massive sulfides produced by conductive cooling underwent limited fractionation of the Zn isotopes. However, there were relatively low  $\delta^{66}\text{Zn}$  values for another massive sulfide sample (S25-21). S25-21 contained many Cu sulfides but little sphalerite. Moreover, the Zn isotopic mass fractionation of different sulfides can result in the enrichment of the light isotopes in Cu sulfides. Consequently, there was a lower Zn isotopic composition in this sample. In addition to S25-21, the mass fractionation effects of different sulfides were seen in S35-17 and S27-4 as well. In these samples, sphalerite-rich subsamples (S27-4-1 and S35-17-2) had higher  $\delta^{66}\text{Zn}$  values than the whole rock and pyrite subsamples (S27-4-2 and S35-17-1; Table 2). However, the Zn-rich massive sulfide sample (S27-4) was characterized by a  $\delta^{66}\text{Zn}$  value lower than those for the other samples. The author used TEM (transmission electron microscopy) and found there were many sphalerite-type stacking faults in the wurtzite of this sample, indicating that wurtzite transformed to sphalerite. Redissolution and transformation between Zn sulfides may be a reason for the  $\delta^{66}\text{Zn}$  decrease.

As indicated by the discussion above, we found that the Zn in the SWIR samples was derived from the mantle, as were the Fe and Cu isotopes. However, there was no obvious fractionation occurring in the leaching processes. The main reason for Zn isotopic fractionation involved sulfides that precipitated rapidly (e.g., S35-17).

#### 5.4. Fe-Cu-Zn Isotopic System in the SWIR

The Fe-Cu-Zn isotopes in the SWIR hydrothermal sulfides were analyzed in this study. We found that the metallic elements, such as Fe, Cu, and Zn, were derived from the mantle. The Fe and Cu isotopic results indicated that these metallic elements were provided to the hydrothermal systems by fluid leaching of the source rocks, which reasonably explains the ore-forming material sources and contribution mechanisms in the SWIR hydrothermal systems. However, did not analyze the Fe-Cu-Zn isotopic compositions of the hydrothermal fluids directly, and the whole isotopic system should be studied further.

Using the Fe-Cu-Zn isotopic fractionation mechanism and the results for the hydrothermal sulfides, we can estimate the isotopic compositions of the hydrothermal fluids. As

far as the Fe isotopes are concerned, conductive cooling led to the formation of massive sulfides through multiple remineralization stages and produced sulfides with  $\delta^{56}\text{Fe}$  values that indicated isotopic equilibrium with the fluids; so, the  $\delta^{56}\text{Fe}$  values of the fluids were consistent with those of the massive sulfides. As a result, the  $\delta^{56}\text{Fe}$  values of the hydrothermal fluids ranged from  $-0.8\text{‰}$  to  $0\text{‰}$ , which was consistent with the Fe isotopic composition of the hydrothermal fluids in the TAG, Rainbow, EPR  $9\text{--}10^\circ\text{N}$ , and Juan de Fuca hydrothermal fields. Because of the limited Cu isotopic fractionation caused by sulfide precipitation, the Cu isotopic compositions in the sulfides represent those in the hydrothermal fluids after excluding the reason for the reworking processes. As a result, the  $\delta^{65}\text{Cu}_{(\text{fluid})}$  values of the hydrothermal fluids may fall within the range of  $1.0$  to  $3.0\text{‰}$  and experience two stages, including  $^{65}\text{Cu}$  enrichment in the early stage and  $^{65}\text{Cu}$  depletion in the late stage. Sulfide precipitation played an important role in Zn isotopic fractionation, but the temperature and source rock did not. Therefore, we back-calculated that the  $\delta^{66}\text{Zn}$  values of the fluids ranged from  $0$  to  $0.48\text{‰}$  and fell within the  $\delta^{66}\text{Zn}$  range for the hydrothermal fluids tested in the TAG and EPR  $13^\circ\text{N}$  and  $21^\circ\text{N}$  hydrothermal fields. Based on the discussion above, the Fe, Cu, and Zn in the SWIR hydrothermal fields were derived from the mantle; the Fe-Cu-Zn isotopic systems in the  $49\text{--}50^\circ\text{E}$  hydrothermal fields from the SWIR are shown in Figure 9.

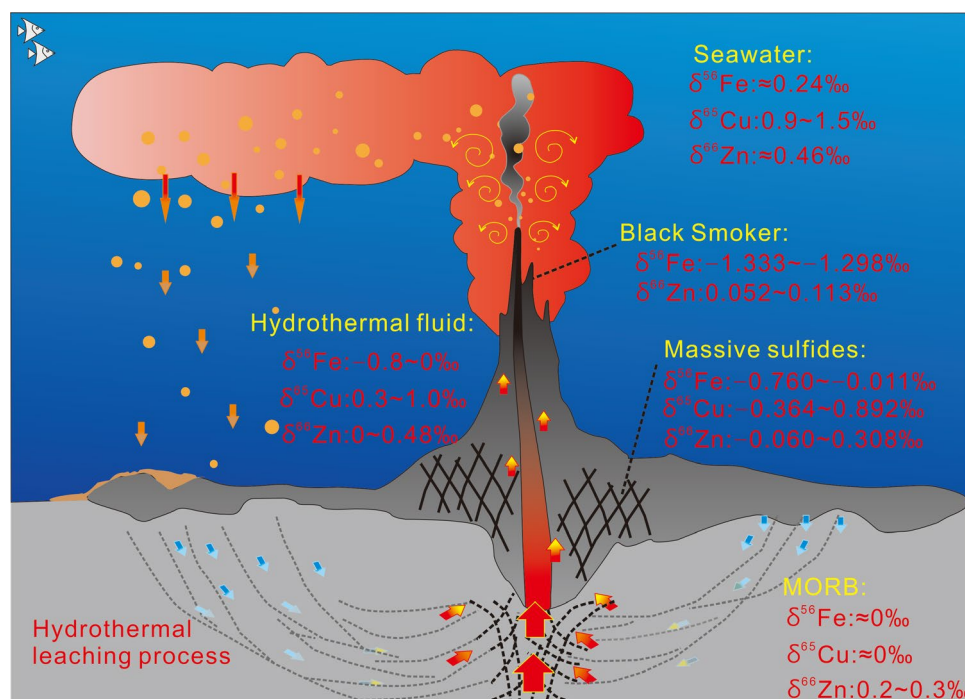


**Figure 9.** Fe-Cu-Zn isotopic compositions of hydrothermal systems in  $49\text{--}50^\circ\text{E}$  from SWIR. Data of basalt were given by Marechal [69,87] and John et al. [88].

## 6. Conclusions

In this study, we analyzed the Fe-Cu-Zn isotopic compositions of hydrothermal sulfides from the SWIR  $49\text{--}50^\circ\text{E}$  hydrothermal fields; the compositions suggested that the metallic elements were derived from the mantle. The Fe and Cu isotope results indicated that these metallic elements were provided to the hydrothermal systems by fluid leaching of the source rock. The potential factors controlling Fe isotopic fractionation in the hydrothermal fluids include the precipitation mechanism, initial isotopic composition, and precipitation temperature. Hydrothermal fluid reworking processes played the most important role in the Cu isotopic fractionation. However, the main reasons for the Zn isotopic fractionation included rapid sulfide precipitation and mass fractionation. Using the Fe-Cu-Zn isotopic fractionation mechanism and the results for the hydrothermal

sulfides, the Fe-Cu-Zn isotopic compositions of the hydrothermal fluids were estimated ( $\delta^{56}\text{Fe}_{(\text{fluid})}$ :  $-0.8\sim 0\text{‰}$ ;  $\delta^{65}\text{Cu}_{(\text{fluid})}$ :  $0.3\sim 1.0\text{‰}$ ;  $\delta^{66}\text{Zn}_{(\text{fluid})}$ :  $0\sim 0.48\text{‰}$ ).

**Author Contributions:** Writing—original draft preparation, Y.W. and Z.W.; writing—review and editing, Y.H. and X.S.; data analysis, F.Y.; resources, J.Y. and Z.Y.; methodology, L.X. All authors have read and agreed to the published version of the manuscript.

**Funding:** This research project was jointly funded by National Natural Science Foundation of China (Grant No. 41503036, 42072084, 41702066, 41273054 and 41602092), the National Key R & D Program of China (2018YFC0309902), the Guangdong Basic and Applied Basic Research Foundation (2019A1515011922), and the Marine economic development project of Guangdong Province (GDNRC [2022]51).

**Data Availability Statement:** There are many types of data, and the quantity is large and complex in this study. Therefore, they are available on request from the corresponding author.

**Acknowledgments:** We gratefully acknowledge the China Ocean Mineral Resources Research and Development Association (COMRA) for providing the hydrothermal sulfide samples.

**Conflicts of Interest:** The authors declare no conflict of interest.

## References

- Hannington, M.D.; Thompson, G.; Rona, P.A.; Scott, S.D. Gold and native copper in supergene sulphides from the Mid-Atlantic Ridge. *Nature* **1988**, *333*, 64–66. [[CrossRef](#)]
- Hannington, M.D.; Scott, S.D. Sulfidation equilibria as guides to gold mineralization in volcanogenic massive sulfides; evidence from sulfide mineralogy and the composition of sphalerite. *Econ. Geol.* **1989**, *84*, 1978–1995. [[CrossRef](#)]
- Hannington, M.D.; Tivey, M.K.; Larocque, A.C.; Petersen, S.; Rona, P.A. The occurrence of gold in sulfide deposits of the TAG hydrothermal field, Mid-Atlantic Ridge. *Can. Mineral.* **1995**, *33*, 1285–1310.
- Herzig, P.M.; Hannington, M.D.; Fouquet, Y.; Von Stackelberg, U.; Petersen, S. Gold-rich polymetallic sulfides from the Lau back arc and implications for the geochemistry of gold in sea-floor hydrothermal systems of the Southwest Pacific. *Econ. Geol.* **1993**, *88*, 2182–2209. [[CrossRef](#)]
- Murphy, P.J.; Meyer, G. A gold-copper association in ultramafic-hosted hydrothermal sulfides from the Mid-Atlantic Ridge. *Econ. Geol.* **1998**, *93*, 1076–1083. [[CrossRef](#)]
- Moss, R.; Scott, S.D. Geochemistry and mineralogy of gold-rich hydrothermal precipitates from the Eastern Manus Basin, Papua New Guinea. *Can. Mineral.* **2001**, *39*, 957–978. [[CrossRef](#)]
- Baker, E.T.; Edmonds, H.N.; Michael, P.J.; Bach, W.; Dick, H.J.B.; Snow, J.E.; Walker, S.L.; Banerjee, N.R.; Langmuir, C.H. Hydrothermal venting in magma deserts: The ultraslow-spreading Gakkel and Southwest Indian Ridges. *Geochem. Geophys. Geosyst.* **2004**, *5*, Q08002. [[CrossRef](#)]
- Tao, C.H.; Li, H.M.; Huang, W.; Han, X.Q.; Wu, G.H.; Su, X.; Zhou, N.; Lin, J.; He, Y.H.; Zhou, J.P. Mineralogical and geochemical features of sulfide chimneys from the 49°39' E hydrothermal field on the Southwest Indian Ridge and their geological inferences. *Chin. Sci. Bull.* **2011**, *56*, 2828. [[CrossRef](#)]
- Georgen, J.E.; Lin, J.; Dick, H.J.B. Evidence from gravity anomalies for interactions of the Marion and Bouvet hotspots with the Southwest Indian Ridge: Effects of transform offsets. *Earth Planet. Sci. Lett.* **2001**, *187*, 283–300. [[CrossRef](#)]
- Sauter, D.; Patriat, P.; Rommevaux-Jestin, C.; Cannat, M.; Briais, A. The Southwest Indian Ridge between 49°15' E and 57° E: Focused accretion and magma redistribution. *Earth Planet. Sci. Lett.* **2001**, *192*, 303–317. [[CrossRef](#)]
- Muller, M.R.; Minshull, T.A.; White, R.S. Segmentation and melt supply at the Southwest Indian Ridge. *Geology* **1999**, *27*, 867–870. [[CrossRef](#)]
- Ye, J.; Shi, X.; Yang, Y.; Liu, J.; Zhou, G.; Li, N. Mineralogy of sulfides from ultraslow spreading Southwest Indian Ridge 49.6 E hydrothermal field and its metallogenic significance. *Acta Mineral. Sin.* **2011**, *31*, 17–29.
- Ji, F.; Zhou, H.; Yang, Q.; Gao, H.; Wang, H.; Lilley, M.D. Geochemistry of hydrothermal vent fluids and its implications for subsurface processes at the active Longqi hydrothermal field, Southwest Indian Ridge. *Deep Sea Res.* **2017**, *122*, 41–47. [[CrossRef](#)]
- Herzig, P.M.; Hannington, M.D. Polymetallic massive sulfides at the modern seafloor a review. *Ore Geol. Rev.* **1995**, *10*, 95–115. [[CrossRef](#)]
- Meyer, G.; Cambon, P.; Etoubleau, J.; Fouquet, Y.; Henry, K.; Murphy, P. Gold-silver mineralization in submarine hydrothermal sulphides: INAA results after ten years of intense prospecting. *J. Radioanal. Nucl. Chem.* **2000**, *244*, 583–587. [[CrossRef](#)]
- Jiang, S.Y. Transition metal isotopes: Analytical methods and geological application. *Earth Sci. Front.* **2003**, *10*, 269–278.
- Maréchal, C.N.; Télouk, P.; Albarède, F. Precise analysis of copper and zinc isotopic compositions by plasma-source mass spectrometry. *Chem. Geol.* **1999**, *156*, 251–273. [[CrossRef](#)]
- Belshaw, N.S.; Zhu, X.K.; Guo, Y.; O'Nions, R.K. High precision measurement of iron isotopes by plasma source mass spectrometry. *Int. J. Mass Spectrom.* **2000**, *197*, 191–195. [[CrossRef](#)]

19. Zhu, X.K.; O’Nions, R.K.; Guo, Y.; Belshaw, N.S.; Rickard, D. Determination of natural Cu-isotope variation by plasma-source mass spectrometry: Implications for use as geochemical tracers. *Chem. Geol.* **2000**, *163*, 139–149. [[CrossRef](#)]
20. Beard, B.L.; Johnson, C.M.; Skulan, J.L.; Neelson, K.H.; Cox, L.; Sun, H. Application of Fe isotopes to tracing the geochemical and biological cycling of Fe. *Chem. Geol.* **2003**, *195*, 87–117. [[CrossRef](#)]
21. Rouxel, O.; Fouquet, Y.; Ludden, J.N. Subsurface processes at the lucky strike hydrothermal field, Mid-Atlantic Ridge: Evidence from sulfur, selenium, and iron isotopes 1 Associate editor: S. Sheppard. *Geochim. Cosmochim. Acta* **2004**, *68*, 2295–2311. [[CrossRef](#)]
22. John, S.G.; Rouxel, O.J.; Craddock, P.R.; Engwall, A.M.; Boyle, E.A. Zinc stable isotopes in seafloor hydrothermal vent fluids and chimneys. *Earth Planet. Sci. Lett.* **2008**, *269*, 17–28. [[CrossRef](#)]
23. Liu, S.A.; Huang, J.; Liu, J.; Wörner, G.; Yang, W.; Tang, Y.J.; Chen, Y.; Tang, L.; Zheng, J.; Li, S. Copper isotopic composition of the silicate earth. *Earth Planet. Sci. Lett.* **2015**, *427*, 95–103. [[CrossRef](#)]
24. Sharma, M.; Polizzotto, M.; Anbar, A.D. Iron isotopes in hot springs along the Juan de Fuca Ridge. *Earth Planet. Sci. Lett.* **2001**, *194*, 39–51. [[CrossRef](#)]
25. Chu, N.C.; Johnson, C.M.; Beard, B.L.; German, C.R.; Nesbitt, R.W.; Frank, M.; Bohn, M.; Kubik, P.W.; Usui, A.; Graham, I. Evidence for hydrothermal venting in Fe isotope compositions of the deep Pacific Ocean through time. *Earth Planet. Sci. Lett.* **2006**, *245*, 202–217. [[CrossRef](#)]
26. Beard, B.L.; Johnson, C.M.; Von Damm, K.L.; Poulson, R.L. Iron isotope constraints on Fe cycling and mass balance in oxygenated earth oceans. *Geology* **2003**, *31*, 629–632. [[CrossRef](#)]
27. Severmann, S.; Johnson, C.M.; Beard, B.L.; German, C.R.; Edmonds, H.N.; Chiba, H.; Green, D.R.H. The effect of plume processes on the Fe isotope composition of hydrothermally derived Fe in the deep ocean as inferred from the Rainbow vent site, Mid-Atlantic Ridge, 36°14’ N. *Earth Planet. Sci. Lett.* **2004**, *225*, 63–76. [[CrossRef](#)]
28. Bennett, S.A.; Rouxel, O.; Schmidt, K.; Garbe-Schönberg, D.; Statham, P.J.; German, C.R. Iron isotope fractionation in a buoyant hydrothermal plume, 5° S Mid-Atlantic Ridge. *Geochim. Cosmochim. Acta* **2009**, *73*, 5619–5634. [[CrossRef](#)]
29. Wang, S.; Sun, W.; Huang, J.; Zhai, S.; Li, H. Coupled Fe–S isotope composition of sulfide chimneys dominated by temperature heterogeneity in seafloor hydrothermal systems. *Sci. Bull.* **2020**, *65*, 1767–1774. [[CrossRef](#)]
30. Zeng, Z.; Li, X.; Chen, S.; De Jong, J.; Mattielli, N.; Qi, H.; Pearce, C.; Murton, B.J. Iron, copper, and zinc isotopic fractionation in seafloor basalts and hydrothermal sulfides. *Mar. Geol.* **2021**, *436*, 106491. [[CrossRef](#)]
31. Teng, F.Z.; Dauphas, N.; Huang, S.; Marty, B. Iron isotopic systematics of oceanic basalts. *Geochim. Cosmochim. Acta* **2013**, *107*, 12–26. [[CrossRef](#)]
32. Moeller, K.; Schoenberg, R.; Grenne, T.; Thorseth, I.H.; Drost, K.; Pedersen, R.B. Comparison of iron isotope variations in modern and Ordovician siliceous Fe oxyhydroxide deposits. *Geochim. Cosmochim. Acta* **2014**, *126*, 422–440. [[CrossRef](#)]
33. Rouxel, O.; Fouquet, Y.; Ludden, J.N. Copper isotope systematics of the lucky strike, rainbow, and logatchev sea-floor hydrothermal fields on the mid-atlantic ridge. *Econ. Geol.* **2004**, *99*, 585–600. [[CrossRef](#)]
34. Mason, T.F.D.; Weiss, D.J.; Chapman, J.B.; Wilkinson, J.J.; Tessalina, S.G.; Spiro, B.; Horstwood, M.S.A.; Spratt, J.; Coles, B.J. Zn and Cu isotopic variability in the Alexandrinka volcanic-hosted massive sulphide (VHMS) ore deposit, Urals, Russia. *Chem. Geol.* **2005**, *221*, 170–187. [[CrossRef](#)]
35. Markl, G.; Lahaye, Y.; Schwinn, G. Copper isotopes as monitors of redox processes in hydrothermal mineralization. *Geochim. Cosmochim. Acta* **2006**, *70*, 4215–4228. [[CrossRef](#)]
36. Kim, J.; Moon, J.; Lee, I.; Kim, Y.; Larson, P. Copper isotope composition of seafloor hydrothermal vents in back-arc and arc settings, Western Pacific. In Proceedings of the Goldschmidt Conference Abstracts, Sacramento, CA, USA, 8–14 June 2014; Geochemical Society and European Association of Geochemistry, 2014; p. 1249.
37. Fernandez, A.; Borrok, D.M. Fractionation of Cu, Fe, and Zn isotopes during the oxidative weathering of sulfide-rich rocks. *Chem. Geol.* **2009**, *264*, 1–12. [[CrossRef](#)]
38. Doucet, L.S.; Mattielli, N.; Ionov, D.A.; Debouge, W.; Golovin, A.V. Zn isotopic heterogeneity in the mantle: A melting control? *Earth Planet. Sci. Lett.* **2016**, *451*, 232–240. [[CrossRef](#)]
39. Samanta, M.; Ellwood, M.J.; Sinoir, M.; Hassler, C.S. Dissolved zinc isotope cycling in the Tasman Sea, SW Pacific Ocean. *Mar. Chem.* **2017**, *192*, 1–12. [[CrossRef](#)]
40. Li, X.; Wang, J.; Chu, F.; Wang, H.; Li, Z.; Yu, X.; Bi, D.; He, Y. Variability of Fe isotope compositions of hydrothermal sulfides and oxidation products at mid-ocean ridges. *J. Mar. Syst.* **2018**, *180*, 191–196. [[CrossRef](#)]
41. Georgen, J.E.; Kurz, M.D.; Dick, H.J.B.; Lin, J. Low <sup>3</sup>He/<sup>4</sup>He ratios in basalt glasses from the Western Southwest Indian Ridge (10°–24° E). *Earth Planet. Sci. Lett.* **2003**, *206*, 509–528. [[CrossRef](#)]
42. Grindlay, N.R.; Madsen, J.A.; Rommevaux-Jestin, C.; Sclater, J. A different pattern of ridge segmentation and mantle Bouguer gravity anomalies along the ultra-slow spreading Southwest Indian Ridge (15°30’ E to 25° E). *Earth Planet. Sci. Lett.* **1998**, *161*, 243–253. [[CrossRef](#)]
43. Li, X.; Chu, F.; Lei, J.; Zhao, J. Advances in slow-ultraslow-spreading Southwest Indian Ridge. *Adv. Earth Sci.* **2008**, *23*, 595–603. [[CrossRef](#)]
44. Li, X.H.; Lei, J.J.; Zhao, J.R. Characteristics of seafloor ultramafic hosted hydrothermal systems and the implications. *Mar. Geol. Quat. Geol.* **2008**, *28*, 133–139.

45. Tao, C.; Lin, J.; Guo, S.; Chen, Y.J.; Wu, G.; Han, X.; German, C.R.; Yoerger, D.R.; Zhou, N.; Li, H.; et al. First active hydrothermal vents on an ultraslow-spreading center: Southwest Indian Ridge. *Geology* **2012**, *40*, 47–50. [[CrossRef](#)]
46. Tao, C.; Li, H.; Jin, X.; Zhou, J.; Wu, T.; He, Y.; Deng, X.; Gu, C.; Zhang, G.; Liu, W. Seafloor hydrothermal activity and polymetallic sulfide exploration on the Southwest Indian Ridge. *Chin. Sci. Bull.* **2014**, *59*, 2266–2276. [[CrossRef](#)]
47. Zhang, T.; Lin, J.; Gao, J. Interactions between hotspots and the Southwest Indian Ridge during the last 90 Ma: Implications on the formation of oceanic plateaus and intra-plate seamounts. *Sci. China Earth Sci.* **2011**, *54*, 1177–1188. [[CrossRef](#)]
48. Zhang, T.; Lin, J.; Gao, J. Magmatism and tectonic processes in Area A hydrothermal vent on the Southwest Indian Ridge. *Sci. China Earth Sci.* **2013**, *56*, 2186–2197. [[CrossRef](#)]
49. Ren, M.; Chen, J.; Shao, K.; Zhang, S. Metallogenic information extraction and quantitative prediction process of seafloor massive sulfide resources in the Southwest Indian Ocean. *Ore Geol. Rev.* **2016**, *76*, 108–121. [[CrossRef](#)]
50. Zhao, M.; Qiu, X.; Li, J.; Sauter, D.; Ruan, A.; Chen, J.; Cannat, M.; Singh, S.; Zhang, J.; Wu, Z.; et al. Three-dimensional seismic structure of the Dragon Flag oceanic core complex at the ultraslow spreading Southwest Indian Ridge (49°39' E). *Geochem. Geophys. Geosyst.* **2013**, *14*, 4544–4563. [[CrossRef](#)]
51. Sun, C.; Wu, Z.; Tao, C.; Ruan, A.; Zhang, G.; Guo, Z.; Huang, E. The deep structure of the Duanqiao hydrothermal field at the Southwest Indian Ridge. *Acta Oceanol. Sin.* **2018**, *37*, 73–79. [[CrossRef](#)]
52. Yang, W.; Tao, C.; Li, H.; Liang, J.; Liao, S.; Long, J.; Ma, Z.; Wang, L. <sup>230</sup>Th/<sup>238</sup>U dating of hydrothermal sulfides from Duanqiao hydrothermal field, Southwest Indian Ridge. *Mar. Geophys. Res.* **2017**, *38*, 71–83. [[CrossRef](#)]
53. Han, X.; Wu, G.; Cui, R.; Qiu, Z.; Deng, X.; Wang, Y. Discovery of a hydrothermal sulfide deposit on the Southwest Indian Ridge at 49.2 E. In Proceedings of the AGU Fall Meeting Abstracts, San Francisco, CA, USA, 13–17 December 2010; American Geophysical Union: Washington, DC, USA, 2010; p. OS21C–1531.
54. Sauter, D.; Carton, H.; Mendel, V.; Munsch, M.; Rommevaux-Jestin, C.; Schott, J.J.; Whitechurch, H. Ridge segmentation and the magnetic structure of the Southwest Indian Ridge (at 50°30' E, 55°30' E and 66°20' E): Implications for magmatic processes at ultraslow-spreading centers. *Geochem. Geophys. Geosyst.* **2004**, *5*, Q05K08. [[CrossRef](#)]
55. Sauter, D.; Cannat, M.; Meyzen, C.; Bezos, A.; Patriat, P.; Humler, E.; Debayle, E. Propagation of a melting anomaly along the ultraslow Southwest Indian Ridge between 46°E and 52°20'E: Interaction with the Crozet hotspot? *Geophys. J. Int.* **2009**, *179*, 687–699. [[CrossRef](#)]
56. Wang, Y.; Wu, Z.; Sun, X.; Deng, X.; Guan, Y.; Xu, L.; Huang, Y.; Cao, K. He–Ar–S isotopic compositions of polymetallic sulphides from hydrothermal vent fields along the ultraslow-spreading Southwest Indian Ridge and their geological implications. *Minerals* **2018**, *8*, 512. [[CrossRef](#)]
57. Pérez Rodríguez, N.; Engström, E.; Rodushkin, I.; Nason, P.; Alakangas, L.; Öhlander, B. Copper and iron isotope fractionation in mine tailings at the Laver and Kristineberg mines, Northern Sweden. *Appl. Geochem.* **2013**, *32*, 204–215. [[CrossRef](#)]
58. Rodushkin, I.; Stenberg, A.; Andrén, H.; Malinovsky, D.; Baxter, D.C. Isotopic fractionation during diffusion of transition metal ions in solution. *Anal. Chem.* **2004**, *76*, 2148–2151. [[CrossRef](#)]
59. Tang, S.; Yan, B.; Zhu, X.; Li, J.; Li, S. Iron, copper and zinc isotopic compositions of basaltic standard reference materials. *Rock Miner. Anal.* **2012**, *31*, 218–224.
60. Rouxel, O.; Shanks, W.C.; Bach, W.; Edwards, K.J. Integrated Fe- and S-isotope study of seafloor hydrothermal vents at East Pacific Rise 9–10° N. *Chem. Geol.* **2008**, *252*, 214–227. [[CrossRef](#)]
61. Zhu, X.K.; O'Nions, R.K.; Guo, Y.; Reynolds, B.C. Secular variation of iron isotopes in North Atlantic deep water. *Science* **2000**, *287*, 2000–2002. [[CrossRef](#)]
62. Johnson, C.M.; Beard, B.L.; Beukes, N.J.; Klein, C.; O'Leary, J.M. Ancient geochemical cycling in the Earth as inferred from Fe isotope studies of banded iron formations from the Transvaal Craton. *Contrib. Mineral. Petrol.* **2003**, *144*, 523–547. [[CrossRef](#)]
63. Bullen, T.D.; White, A.F.; Childs, C.W.; Vivit, D.V.; Schulz, M.S. Demonstration of significant abiotic iron isotope fractionation in nature. *Geology* **2001**, *29*, 699–702. [[CrossRef](#)]
64. Beard, B.L.; Johnson, C.M.; Cox, L.; Sun, H.; Neelson, K.H.; Aguilar, C. Iron isotope biosignatures. *Science* **1999**, *285*, 1889–1892. [[CrossRef](#)] [[PubMed](#)]
65. Brantley, S.L.; Liermann, L.; Bullen, T.D. Fractionation of Fe isotopes by soil microbes and organic acids. *Geology* **2001**, *29*, 535–538. [[CrossRef](#)]
66. Luther, G.W.; Rozan, T.F.; Taillefert, M.; Nuzzio, D.B.; Di Meo, C.; Shank, T.M.; Lutz, R.A.; Cary, S.C. Chemical speciation drives hydrothermal vent ecology. *Nature* **2001**, *410*, 813–816. [[CrossRef](#)]
67. Wang, Y.; Sun, X.M.; Xu, L.; Liang, Y.H.; Wu, Z.W.; Fu, Y.; Huang, Y. In situ analysis of element geochemistry in submarine basalt in hydrothermal areas from ultraslow spreading Southwest Indian Ridge. *Spectrosc. Spectr. Anal.* **2015**, *35*, 796–802. [[CrossRef](#)]
68. Butler, I.B.; Nesbitt, R.W. Trace element distributions in the chalcopyrite wall of a black smoker chimney: Insights from laser ablation inductively coupled plasma mass spectrometry (LA-ICP-MS). *Earth Planet. Sci. Lett.* **1999**, *167*, 335–345. [[CrossRef](#)]
69. Marechal, C.; Albarede, F.; Telouk, P. Natural copper and zinc isotopic compositions measured by Plasma-Source Mass Spectrometry. *Mineral. Mag. A* **1998**, *62*, 947–948. [[CrossRef](#)]
70. Bermin, J.; Vance, D.; Archer, C.; Statham, P.J. The determination of the isotopic composition of Cu and Zn in seawater. *Chem. Geol.* **2006**, *226*, 280–297. [[CrossRef](#)]
71. Savage, P.S.; Moynier, F.; Chen, H.; Shofner, G.; Siebert, J.; Badro, J.; Puchtel, I. Copper isotope evidence for large-scale sulphide fractionation during Earth's differentiation. *Geochem. Perspect. Lett.* **2015**, *1*, 53–64. [[CrossRef](#)]

72. Dekov, V.; Rouxel, O. Cu-and Zn-isotope systematics of seafloor hydrothermal vent fluids from a back-arc setting (Manus Basin). In Proceedings of the EGU General Assembly Conference Abstracts, Vienna, Austria, 22–27 April 2012; European Geosciences Union: Munich, Germany, 2012; p. 13020.
73. Vance, D.; Archer, C.; Bermin, J.; Perkins, J.; Statham, P.J.; Lohan, M.C.; Ellwood, M.J.; Mills, R.A. The copper isotope geochemistry of rivers and the oceans. *Earth Planet. Sci. Lett.* **2008**, *274*, 204–213. [[CrossRef](#)]
74. Little, S.H.; Vance, D.; Walker-Brown, C.; Landing, W.M. The oceanic mass balance of copper and zinc isotopes, investigated by analysis of their inputs, and outputs to ferromanganese oxide sediments. *Geochim. Cosmochim. Acta* **2014**, *125*, 673–693. [[CrossRef](#)]
75. Borrok, D.M.; Nimick, D.A.; Wanty, R.B.; Ridley, W.I. Isotopic variations of dissolved copper and zinc in stream waters affected by historical mining. *Geochim. Cosmochim. Acta* **2008**, *72*, 329–344. [[CrossRef](#)]
76. Larson, P.B.; Maher, K.; Ramos, F.C.; Chang, Z.; Gaspar, M.; Meinert, L.D. Copper isotope ratios in magmatic and hydrothermal ore-forming environments. *Chem. Geol.* **2003**, *201*, 337–350. [[CrossRef](#)]
77. Li, Z.; Yang, Z.; Zhu, X.; Hou, Z.; Li, S.; Li, Z.; Wang, Y. Cu isotope composition of Qulong porphyry Cu deposit, Tibet. *Acta Geol. Sin.* **2009**, *83*, 1985–1996.
78. Jiang, S.; Woodhead, J.; Yu, J.; Pan, J.; Liao, Q.; Wu, N. A reconnaissance of Cu isotopic compositions of hydrothermal vein-type copper deposit Jinman, Yunnan, China. *Chin. Sci. Bull.* **2001**, *47*, 249–251. [[CrossRef](#)]
79. Lu, J.J.; Guo, W.M.; Chen, W.F.; Jiang, S.Y.; Li, J.; Yan, X.R.; Xu, Z.W. A metallogenic model for the Dongguashan Cu-Au deposit of Tongling, Anhui Province. *Acta Petrol. Sin.* **2008**, *24*, 1857–1864.
80. Wang, Y.; Zhu, X. Applications of Cu isotopes on studies of mineral deposits: A status report. *J. Jilin Univ.* **2010**, *40*, 739–751.
81. Asael, D.; Matthews, A.; Bar-Matthews, M.; Halicz, L. Copper isotope fractionation in sedimentary copper mineralization (Timna Valley, Israel). *Chem. Geol.* **2007**, *243*, 238–254. [[CrossRef](#)]
82. Wang, Y.; Sun, X.M.; Wu, Z.W.; Deng, X.G.; Dai, Y.Z.; Lin, Z.Y. The enrichment characteristic and mechanism of gold-silver minerals in submarine hydrothermal sulfides from the ultra-slow-spreading SWIR. *Spectrosc. Spectr. Anal.* **2014**, *34*, 3327–3332. [[CrossRef](#)]
83. Seo, J.H.; Lee, S.K.; Lee, I. Quantum chemical calculations of equilibrium copper (I) isotope fractionations in ore-forming fluids. *Chem. Geol.* **2007**, *243*, 225–237. [[CrossRef](#)]
84. Nie, L.; Li, Z.; Fang, X. Cu isotope fractionation during magma evolution process of Qulong Porphyry copper deposit, Tibet. *Miner. Depos.* **2012**, *31*, 718–726.
85. Yang, K.; Scott, S.D. Magmatic degassing of volatiles and ore metals into a hydrothermal system on the modern sea floor of the Eastern Manus Back-Arc Basin, Western Pacific. *Econ. Geol.* **2002**, *97*, 1079–1100. [[CrossRef](#)]
86. Jiang, S.Y.; Ling, H.F.; Yang, J.H.; Zhao, K.D.; Ni, P. New isotopic tracers for hydrothermal mineralization and ore genesis studies and direct dating methods of ore deposits. *Miner. Depos.* **2002**, *21*, 974–976.
87. Maréchal, C.N.; Nicolas, E.; Douchet, C.; Albarède, F. Abundance of zinc isotopes as a marine biogeochemical tracer. *Geochem. Geophys. Geosyst.* **2000**, *1*, 1015. [[CrossRef](#)]
88. John, S.; Bergquist, B.; Saito, M.; Boyle, E. Zinc isotope variations in phytoplankton and seawater. *Geochim. Cosmochim. Acta Suppl.* **2005**, *69*, A546.
89. Debret, B.; Beunon, H.; Mattielli, N.; Andreani, M.; Ribeiro da Costa, I.; Escartin, J. Ore component mobility, transport and mineralization at mid-oceanic ridges: A stable isotopes (Zn, Cu and Fe) study of the Rainbow massif (Mid-Atlantic Ridge 36°14' N). *Earth Planet. Sci. Lett.* **2018**, *503*, 170–180. [[CrossRef](#)]
90. Wang, Z.Z.; Liu, S.A.; Liu, J.; Huang, J.; Xiao, Y.; Chu, Z.Y.; Zhao, X.M.; Tang, L. Zinc isotope fractionation during mantle melting and constraints on the Zn isotope composition of Earth's upper mantle. *Geochim. Cosmochim. Acta* **2017**, *198*, 151–167. [[CrossRef](#)]
91. Zhao, Y.; Vance, D.; Abouchami, W.; De Baar, H.J.W. Biogeochemical cycling of zinc and its isotopes in the Southern Ocean. *Geochim. Cosmochim. Acta* **2014**, *125*, 653–672. [[CrossRef](#)]
92. Archer, C.; Vance, D.; Butler, I.; Butler, I. Abiotic Zn isotope fractionations associated with ZnS precipitation. *Geochim. Cosmochim. Acta* **2004**, *68*, A325.
93. Wilkinson, J.J.; Weiss, D.J.; Mason, T.F.D.; Coles, B.J. Zinc isotope variation in hydrothermal systems: Preliminary evidence from the Irish Midlands Ore Field. *Econ. Geol.* **2005**, *100*, 583–590. [[CrossRef](#)]

**Disclaimer/Publisher's Note:** The statements, opinions and data contained in all publications are solely those of the individual author(s) and contributor(s) and not of MDPI and/or the editor(s). MDPI and/or the editor(s) disclaim responsibility for any injury to people or property resulting from any ideas, methods, instructions or products referred to in the content.